Open Ceramics 10 (2022) 100252

Contents lists available at ScienceDirect

Open Ceramics

journal homepage: www.sciencedirect.com/journal/open-ceramics

Optimisation of trabecular bone mimicking silicon-hydroxyapatite based composite scaffolds processed through selective laser melting

Antonia Ressler [a,*], Nikhil Kamboj [b,c,**], Hrvoje Ivanković [a], Irina Hussainova [b]

[a] Faculty of Chemical Engineering and Technology, University of Zagreb, HR-10000, Zagreb, Marulićev trg 19, Croatia
[b] Tallinn University of Technology, Department of Mechanical and Industrial Engineering, Ehitajate 5, 19086, Tallinn, Estonia
[c] Turku Clinical Biomaterials Centre-TCBC, Department of Biomaterials Science, Faculty of Medicine, Institute of Dentistry, University of Turku, FI-20014, Turku, Finland

ARTICLE INFO

Keywords:
Bone regeneration
Hydroxyapatite
Larnite
Scaffold
Selective laser melting
Wollastonite

ABSTRACT

Additive manufacturing is a rapid prototyping technology to produce complex three-dimensional scaffolds suitable for personalized medicine. In the present study, the laser powder bed fusion through a selective laser melting (SLM) approach has been applied to optimized fabrication of bio-mimicking scaffolds by using hydroxyapatite (HAp, 50 and 70 wt%) and silicon powder mixture. *In situ* formation of pseudo-wollastonite (P–W, $CaSiO_3$) has been detected along with silicon for 50 wt% of HAp powder mixture, while an increase in HAp content has resulted in P–W, silicon and larnite (Ca_2SiO_4) formation. The pore size of 400 μm, according to the CAD model, are observed at the scaffolds fabricated at the shortest exposure time (50 μs), lowest laser current (500 mA) and energy density (41.6 J/mm^3), and simultaneously at the highest scanning speed. Compressive stress demonstrated by the fabricated scaffolds is shown to be acceptable for their use in metaphyseal region of long bones.

1. Introduction

Bone grafting is one of the most common used surgical methods for bone regeneration in orthopedic procedures and the second most frequent tissue transplantation after blood transfusion [1]. According to the epidemiological study, in 2010–2025, the incidence of fractures in Europe increased at an annual rate of 28%, with an additional 25% economic burden, drawing extensive attention to bone repair medicine research [2]. Due to the growing demand, a major focus of studies is the development of bone grafts, that can replace traditional approaches, including autologous and allogenic bone grafts that are still considered as a gold standard in bone tissue engineering [1,3].

Conventional methods of bone scaffolds fabrication are not capable of producing highly complex structures with detailed features needed for efficient bone regeneration. In contrast, new additive manufacturing (AM) technologies are rapid prototyping technologies for a short time manufacturing of complex three-dimensional (3D) parts without using any molds. In AM approach, a computer-aided design (CAD) of the substrate is needed to create a model to be sliced into a series of 2D cross-sectional layers [4]. The AM technologies allow the fabrication of personalized scaffolds according to the patient bone defect and requirements, and the development of a highly required custom-made approach in the field of regenerative medicine for both long-bone or critical size defects [5]. One of AM methods is a selective laser melting (SLM), which initially was developed for the fabrication of metal scaffolds by using high energy density laser to fulfill a complete melting/-solidification process resulting in superior mechanical strength of the scaffold that is appropriate for the long-bone defects [6]. SLM technique was used to prepare substrates based on non-biodegradable (e.g. 316L stainless steel, pure titanium and titanium alloy, NiTi and Co–Cr alloys) and biodegradable (iron, magnesium, zinc) metals [7]. The materials for a bone scaffold fabrication have to be carefully selected as many metals suffer from lack of biocompatibility, high corrosion rate, scaffold rejection, etc. It is essential to improve the metal scaffold properties to minimize the disadvantages [3]. The scaffold for the bone regeneration should mimic natural features of the bone and, at the same time, should be biocompatible, bioactive and biodegradable, osteoconductive and osteoinductive, providing open porosity to allow diffusion of nutrients, oxygen, metabolic waste, allow seeding and migration of cells, and, consequently, vascularization of the scaffold. In addition, the scaffold

* Corresponding author. Faculty of Chemical Engineering and Technology, University of Zagreb, HR-10000, Zagreb, Marulićev trg 19, p.p.177, Croatia.
** Corresponding author. Tallinn University of Technology, Department of Mechanical and Industrial Engineering, Ehitajate 5, 19086, Tallinn.
E-mail addresses: aressler@fkit.hr (A. Ressler), nikhil.kamboj@taltech.ee (N. Kamboj), hivan@fkit.hr (H. Ivanković), irina.hussainova@taltech.ee (I. Hussainova).

https://doi.org/10.1016/j.oceram.2022.100252
Received 11 January 2022; Received in revised form 9 March 2022; Accepted 31 March 2022
Available online 4 April 2022

should have suitable strength and toughness to facilitate bone repair through remodeling and regeneration [8].

The biocompatibility and osteogenic properties of metal scaffolds can be improved by the addition of bioceramics (e.g. calcium phosphates, calcium silicates) into the metallic powder bed [8–10]. In our previous research, to increase biocompatibility and osteogenic properties of metal scaffolds, wollastonite ($CaSiO_3$) was added along with silicon to fabricate a highly porous composite scaffold with a pore size of 400 μm through the SLM technique [8,9]. It is widely accepted that the porous silicon scaffolds demonstrate an enhanced collagen type I (COL I) expression by facilitating osteoblasts adhesion, while it is determined that COLL I expression increased drastically in the human osteoblasts supplemented by silicon due to orthosilicic acid [11,12]. Silicon enhances the production of proline (hexosamine) related to bone growth through an endochondral ossification and might play a major role in the upregulation of the vascular endothelial growth factor (VEGF) through molecular interaction pathways in endothelial cells and fibroblasts [13,14]. Furthermore, silicon has even undermined the role of calcium at the metaphyseal region and epiphyseal plate, which are developing regions of the bone with a prominent osteoblastic activity [15,16].

Wollastonite is a naturally occurring calcium silicate mineral and is often used as filler in ceramic-ceramic and ceramic-polymer composite scaffolds. The hydrophilic nature of the wollastonite facilitates the apatite layer formation promoting wollastonite usage for bone regenerative applications. The fabricated scaffold based on silicon and wollastonite has shown good biocompatibility and characteristic bone markers expression after 21 days of human mesenchymal stem cell culture [8]. Calcium phosphates (CaP), mainly hydroxyapatite (HAp, $Ca_{10}(PO_4)_6(OH)_2$), are widely used for bone regenerative applications. From a chemical and structural perspective, HAp is analogous to the mineralogical phase of the natural bone tissue [17]. The introduction of CaPs as a bioactive component within the inert metals, often used for the fabrication of scaffolds by the SLM process, can increase osteogenic properties *in vitro* and *in vivo* and the regenerative potential of the scaffolds. On the ceramic counterpart, the addition of silicon to the crystal structure of HAp can potentially enhance the osteoblast differentiation, increase alkaline phosphatase and transcription factors expression and, therefore, boost bone-bonding ability [18,19]. However, the fabrication of CaP bioceramics by the SLM and/or selective laser sintering (SLS) is a challenging procedure since the impact of the laser on the powder bed may result in excessive grain growth, additional phase formation (e.g. calcium oxide, tricalcium phosphates) and decomposition at high temperature. These limitations are the reasons for limited studies [5,20–22].

The objective of the present study was to understand the influence of the HAp phase (50 and 70 wt%) along with osteostimulatory silicon in the powder bed on the phase formation and morphology of the fabricated porous scaffolds. The design of the experiments, considering the effect of process parameters on the morphology, *in situ* phase formation, and mechanical properties were carefully studied on the silicon-hydroxyapatite composite powder bed. To the author's best knowledge, the fabrication of silicon-hydroxyapatite scaffold by SLM and its properties has not been yet reported elsewhere. This novel bone-mimicking scaffold particularly finds its application in the metaphyseal region of the long bones since silicon enhances bone formation through osteochondral ossification and simultaneously provides the required strength.

2. Materials and methods

2.1. Hydroxyapatite precipitation and powder feedstock

Hydroxyapatite was synthesized by the wet precipitation method by dissolving the appropriate amount of calcium oxide (CaO) as a source of Ca^{2+} ions in demineralized water. Ammonium dihydrogen phosphate ($NH_4H_2PO_4$) was added into the solution to gain a Ca/P molar ratio of 1.67 (stoichiometric HAp) according to Eg. 1. Stirring was continued for 3 days at 60 °C followed by overnight aging at room temperature (T = 23.20 ± 0.45 °C) and filtration. The synthesized HAp powder was dried for 24 h at 105 °C.

$$10CaCO_3 + 6(NH_4)_2HPO_4 + 2H_2O \rightarrow Ca_{10}(PO_4)_6(OH)_2 + 6(NH_4)_2CO_3 + 4H_2CO_3 \quad (1)$$

The used materials were powder mixtures of (i) 50 wt% of silicon and 50 wt% of HAp, and (ii) 30 wt% of silicon and 70 wt% of HAp. The powder mixtures of silicon (>99.9% purity, particle size range 10–44 μm, Silgrain-Elkem) and HAp (particle size range 5–40 μm) were mixed in the Turbula® shaker for 3 h with ethanol (96 wt%) using ZrO_2 balls. The obtained mixtures were dried for 24 h at 120 °C.

2.2. Scaffold design

The 3D scaffolds of 5 mm in diameter and 6 mm in height were designed with the help of a CAD by using SOLIDWORKS® (Dassault System, USA) to have the pore diameters of 400 μm as shown in Fig. 1a, b.

2.3. Scaffold fabrication

The 3D scaffolds, based on silicon and HAp, were fabricated by a metal 3D printer using a commercial ReaLizer GmbH SLM-50 (Germany) SLM system. The previously optimized parameters of a layer thickness of 25 μm, hatch distance of 60 μm, and point distance of 10 μm under the impact of Nd^{3+}:YAG laser were applied for the fabrication of scaffolds [8]. The layer thickness of 25 μm is selected since the particle size has several repercussions on the regulation of the immune response by modulating the ionic microenvironment between the scaffolds and the site of implantation. To determine how an exposure time and a laser current affect a crystalline phase content, morphology, and mechanical properties, the parameters were varied according to Table 1. In addition, in Table 1, the samples annotation for both mixtures and different fabrication parameters are described. In order to avoid a severe oxidation of the phases during SLM process, the scaffolds processing was performed under the inert conditions by using high purity argon (99.999 vol%). During the fabrication, a rubber wiper was spreaded over the platform. After fabrication, the loose powder adhered on the surface and in the pores of the scaffolds was removed by a sonication process in ethanol (96 wt%) for 15 min.

2.4. Scaffold characterization

Phase analysis was accomplished using X-ray diffraction analysis (XRD) performed on Shimadzu XRD-6000 diffractometer with Cu K_α (1.5406 Å) radiation, operating at 40 kV and 30 mA, with a 2θ range of 20–70°, at a step size of 0.02° and an exposure of 3s. Prior to phase analysis of the as-prepared HAp powder, the 5 wt% of polycrystalline silicon standard (NIST SRN 640e, Sigma Aldrich) was added to the powder. Software DIFFRAC.SUITE TOPAS V.5.0. (Bruker) with the fundamental parameters approach was employed for Rietveld refinements to determine phase content as the function of different weight percentages of HAp in a feedstock mixture and printing parameters. The structure parameters of HAp, given by Vaselinović et al. [23], silicon by Elliot [24], pseudo-wollastonite (P–W) given by Yeng and Prewitt [25] and larnit by Tsurumi et al. [26] have been used as the initial values in the refinements. The weighted profile (R_{wp}) and expected (R_{exp}) R-factors were used to assess the degree of the match between the calculated pattern and the experimental data. The values of $R_{wp} < 12\%$ and $R_{exp} < 3\%$ were considered as acceptable ones.

The fabricated cylindrical porous scaffolds were tested under compression at an applied strain rate of 0.5 mm min^{-1} using the servo-hydraulic model 8500 universal testing machine (Instron Itd., UK). The

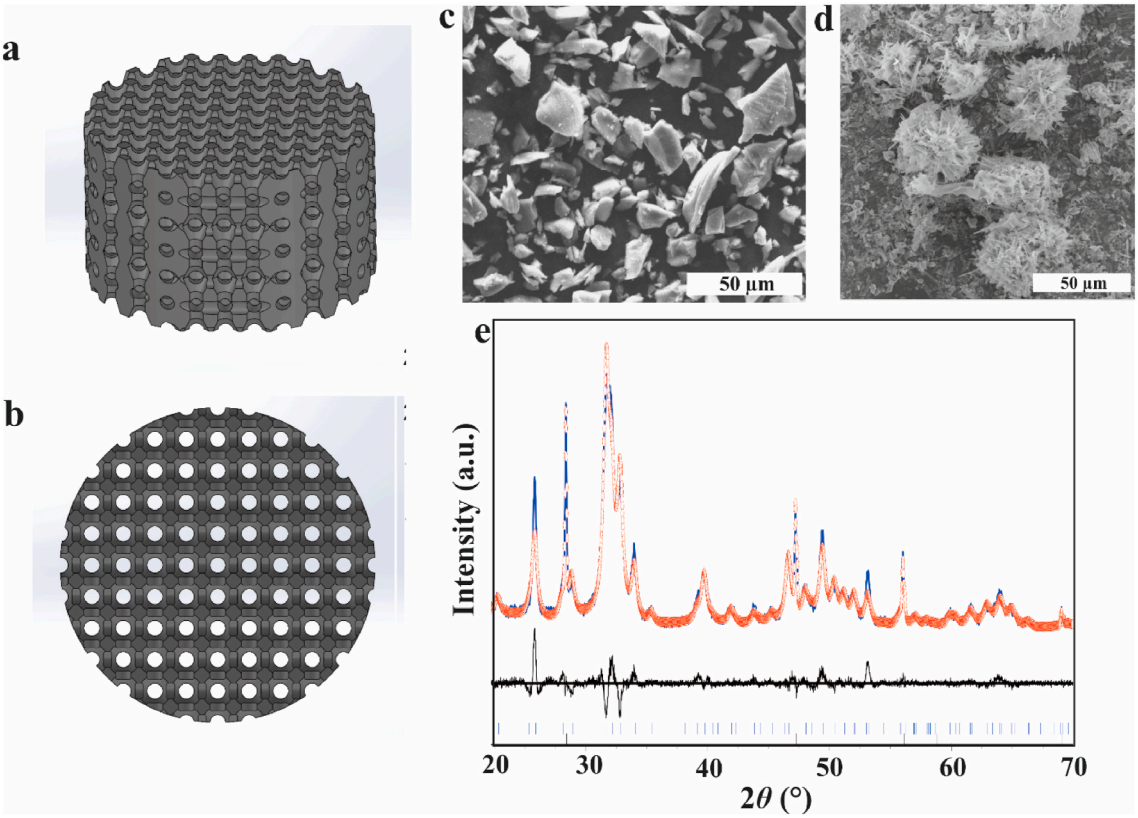

Fig. 1. CAD 3D design of the scaffolds (a) and design of pores (b). Microstructure of the precursor particles: silicon (c) and hydroxyapatite (d). Rietveld analysis pattern of powder diffraction data for HAp powder (e). The open circles (red) are experimental data and the solid lines (blue) are calculated intensities. The difference between the experimental and calculated intensities is plotted below the profile ($R_{wp} < 12\%$; $R_{exp} < 3\%$). Bragg positions of hydroxyapatite and silicon (standard) are marked below each pattern. (For interpretation of the references to colour in this figure legend, the reader is referred to the Web version of this article.)

Table 1
Process optimisation parameters for silicon-hydroxyapatite powder bed.

Exposure time (µs)	120	100	90	80	70	60	50
Laser current (mA)	1200	1000	900	800	700	600	500
Scanning speed (mm/s)	83.3	100.0	111.1	125.0	142.8	166.6	200.0
Energy density (J/mm^3)	241.9	166.0	135.5	111.1	83.3	60.2	41.6
50/50 mixture	50/50_1	50/50_2	50/50_3	50/50_4	50/50_5	50/50_6	50/50_7
30/70 mixture	30/70_1	30/70_2	30/70_3	30/70_4	30/70_5	30/70_6	30/70_7

compressive load and displacement were recorded at 0.1 s intervals during testing. All the compressive strength measurements on the scaffolds were performed at room temperature (T = 22.30 ± 0.25 °C).

The scaffolds morphology before and after the compressive test was analyzed by scanning electron microscopy (SEM, TESCAN Vega3 EasyProbe) at electron beam energy of 13 keV. Scaffolds were coated with the plasma of gold and palladium for 120 s prior to imaging.

2.5. Statistical analysis

Compressive strengths are expressed as a mean ± SD and all measurements were performed on triplicates (n = 3). Statistical analysis was performed using a one-way analysis of variance test to determine significant differences. A value of $p < 0.01$ was considered statistically significant.

3. Results and discussions

In our previous study [8,9], for the first time, the novel scaffold combining osteoconductive, osteoinductive and bioactive elements was successfully applied to the AM of the biomimetic substrates for potential use in bone tissue engineering. The metalloid/ceramic porous scaffolds were manufactured exploiting the approach of SLM. Induction of the primary transcription factors for osteogenic differentiation was detected, indicating the osteogenic properties of scaffolds based on silicon and wollastonite. Furthermore, detection of the anti-inflammatory factors demonstrated the possible immunomodulation effect [8]. In the present study, HAp particles were incorporated into a silicon powder feedstock as a bioactive component aiming at enhanced biological performance. The precursor powders are shown in Fig. 1c,d. Silicon particles are of irregular shape, while plate-like HAp crystals are organized in the flower shape agglomerates. Silicon provides a suitable absorptivity for the Nd:YAG laser, osteoinductivity of the scaffold, mechanical strength, printability in a single-step technology and a bio-interface to support osteoblasts [8]. HAp was obtained by wet precipitation method and the Rietveld refinement analysis of the powder XRD pattern (Fig. 1e) indicated a significant amount of amorphous calcium phosphate (ACP) phase of 14.41 wt%, while the rest of 85.59 wt% is assigned to the HAp phase. The observed XRD pattern and ACP formation along with HAp phase are characteristic for the wet precipitation method at mild

conditions (pH, temperature, atmospheric pressure). SLM technique was implemented for porous composite scaffolds fabrication by using different weight percentages mixtures of silicon and HAp powders within the powder bed.

3.1. Scaffold phase composition

Comparing the experimental diffraction patterns of scaffolds fabricated by using powders containing 50 wt% of silicon and 50 wt% of HAp to the ICDD standards, the crystalline phases were ascribed to silicon (ICDD 27-1402) and P–W (ICDD 74-0874). No peak characteristic for nominally added HAp or other CaP phases was detected. This can be attributed to the thermal instability of the stoichiometric HAp under the impact of the Nd:YAG laser. The stoichiometric HAp is stable until 800 °C, followed by the dehydration and formation of oxyapatite from the temperature ranging 800–1300 °C, according to Eq. (2) [27]:

$$Ca_{10}(PO_4)_6(OH)_2\ (s) \rightarrow Ca_{10}(PO_4)_6O\ (s) + H_2O\ (l) \quad (2)$$

The intercalated water molecules near to the vicinity of the melt pool and between the grains can eventually lead to the hydrolysis of the silicon particles present in the powder bed according to Eq. (3) [28]:

$$Si\ (s) + 2H_2O\ (l) \rightarrow SiO_2\ (s) + 2H_2\ (g) \quad (3)$$

Decomposition of the oxyapatite between 1300 and 1600 °C leads to the formation of tetracalcium phosphate (TTCP) and tricalcium phosphate (TCP, $Ca_3(PO_4)_2$) according to Eq. (4) [29]:

$$Ca_{10}(PO_4)_6O\ (s) \rightarrow Ca_4(PO_4)_2O\ (s) + 2Ca_3(PO_4)_2\ (s) \quad (4)$$

Lastly, decomposition of TTCP leads to the formation of calcium oxide (CaO) and TCP above 1600 °C in accordance to Eq. (5) [27]:

$$Ca_4(PO_4)_2O\ (s) \rightarrow CaO\ (s) + 2Ca_3(PO_4)_2\ (s) \quad (5)$$

The *in situ* reaction of CaO, SiO_2 and $Ca_3(PO_4)_2$ as the products of thermal decomposition of HAp in presence of silicon is very possible during the laser treatment of the powders. The *in situ* reaction leads to the formation of P–W ($CaSiO_3$) according to Eqs. (6) and (7) due to the interaction of powder with the Nd:YAG laser at temperatures above 1600 °C.

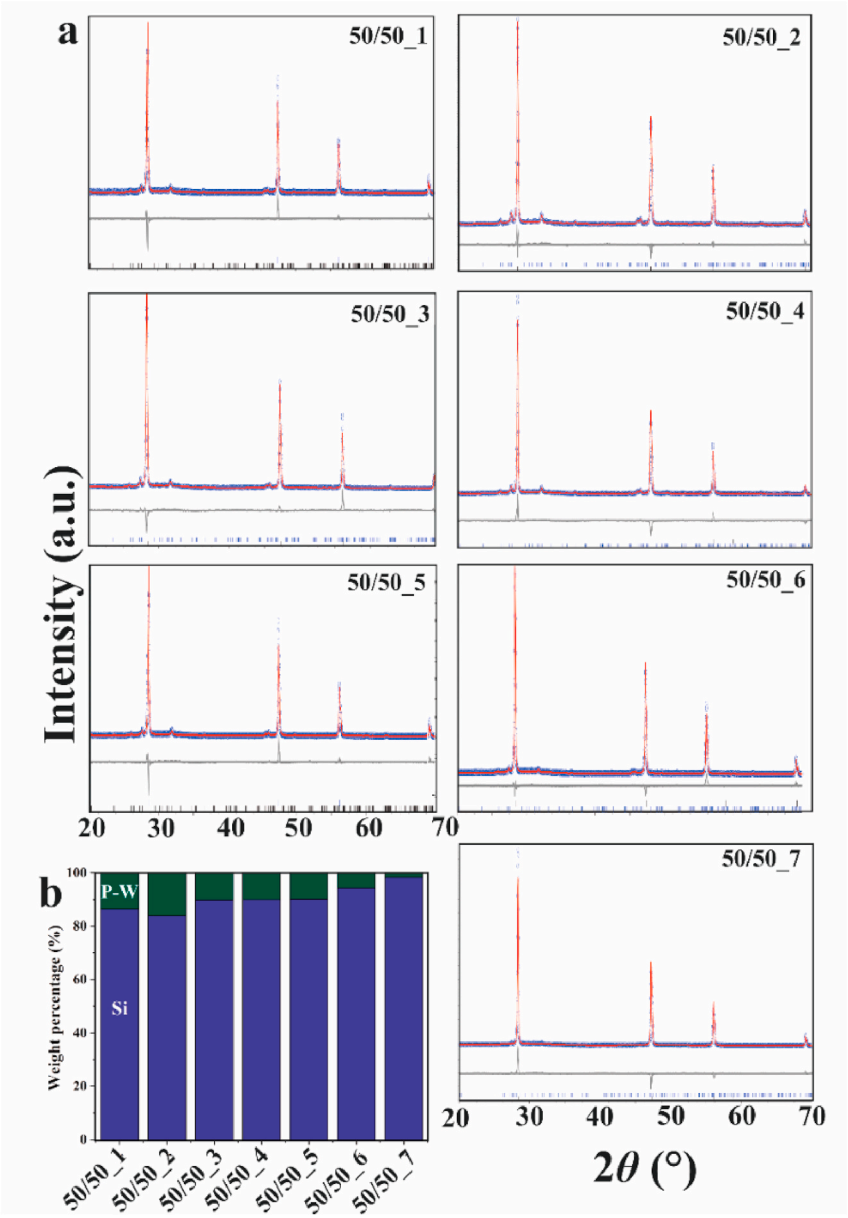

Fig. 2. Rietveld refinement analysis of the powder X-ray diffraction analysis patterns diffraction data for scaffolds with 50 wt% of silicon and 50 wt% of HAp (a) and semi-quantitative analysis of crystalline phases in fabricated scaffolds (b). The open circles (red) are experimental data and the solid lines (blue) are calculated intensities. The difference between the experimental and calculated intensities is plotted below the profile ($R_{wp} < 12\%$; $R_{exp} < 3\%$). Bragg positions of P–W and silicon are marked below each pattern. (For interpretation of the references to colour in this figure legend, the reader is referred to the Web version of this article.)

$$CaO\ (s) + SiO_2\ (s) \rightarrow CaSiO_3\ (s) \quad (6)$$

$$2Ca_3(PO_4)_2\ (s) + 6SiO_2\ (s) \rightarrow 2P_2O_5\ (g) + 6CaSiO_3\ (s) \quad (7)$$

Phosphorus pentoxide (P_2O_5) usually sublimates at 1400–1600 °C allowing *in situ* formation of P–W in the powder bed [30]; however, further analysis is needed for the confirmation of P_2O_5 sublimation. P–W is a high temperature polymorph of wollastonite, which is usually formed at ~1450 °C [31]. Known formation temperatures of P_2O_5 and P–W confirm that the temperature in the powder bed has exceeded 1600 °C making the *in situ* P–W formation possible.

The Rietveld refinement analysis of the powders' XRD patterns (Fig. 2a) and associated weight percentages of crystalline phases (Fig. 2b) indicate a significant amount of newly formed P–W phase. With a decrease of exposure time and laser current, the weight percentage of the P–W phase decreases. The weight percentage of P–W in sample 50/50_1 is 13.55 wt%, while for the sample 50/50_7 is 1.76 wt%. The weight percentage of the *in situ* formed P–W can be correlated with the scanning speed. A lower scanning speed of 83.3 mm/s leads to the highest weight percentage of formed P–W supposing that the longer time of powder – laser interaction allows the reaction to be completed. On the contrary, the scanning speed of 200 mm/s results in the lowest amount of formed P–W.

Comparing the experimental diffraction patterns of scaffolds fabricated by using powders containing 30 wt% of silicon and 70 wt% of HAp to the ICDD standards, the crystalline phases were ascribed to silicon (ICDD 27-1402), P–W (ICDD 74-0874) and larnite (ICDD 09-351). No peak characteristic for nominally added HAp or other CaP phases were

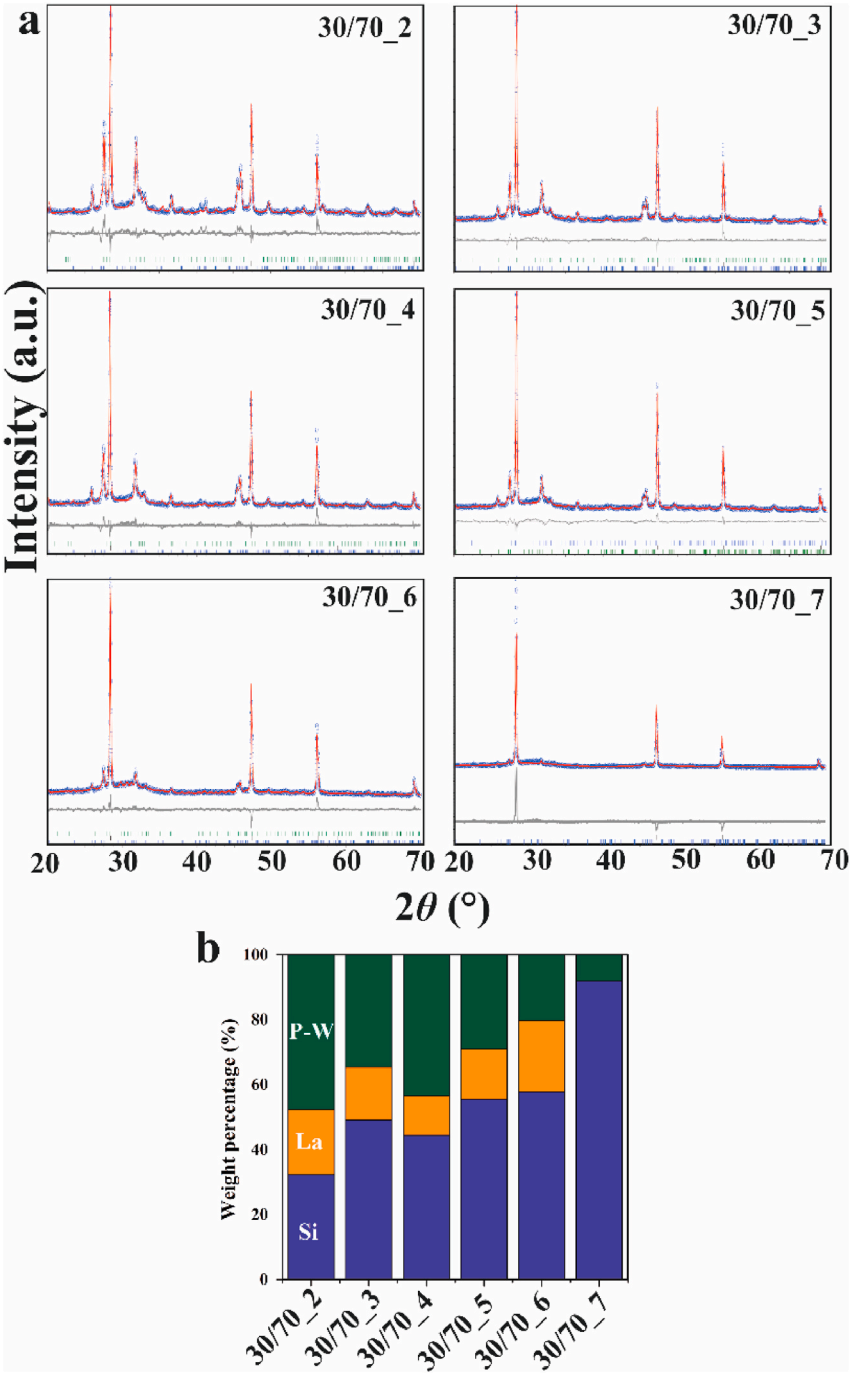

Fig. 3. Rietveld refinement analysis of the powder X-ray diffraction analysis patterns diffraction data for scaffolds with 70 wt% of HAp and 30 wt% of Si (a) and semi-quantitative analysis of crystalline phases in fabricated scaffolds (b). The open circles (red) are experimental data and the solid lines (blue) are calculated intensities. The difference between the experimental and calculated intensities is plotted below the profile (Rwp <12%; Rexp <3%). Bragg positions of P–W, larnite (La) and silicon are marked below each pattern. (For interpretation of the references to colour in this figure legend, the reader is referred to the Web version of this article.)

detected, which reflects the thermal instability of the added HAp phase with the laser interaction. The chosen parameters of processing did not allow the successful fabrication of the scaffold 30/70_1. The Rietveld refinement analysis of the powders' XRD patterns (Fig. 3a) and associated weight percentages of crystalline phases (Fig. 3b), indicates the formation of the P–W phase with additional formed dicalcium silicate phase, larnite (La, Ca_2SiO_4). The *in situ* formation of larnite in the powder bed can be explained according to Eqs. (6) and (7). Larnite is a compound having a twice higher molar ratio of Ca/Si compared to the P–W phase and a higher molar ratio of CaO obtained from HAp decomposition in the powder feedstock can favour larnite formation. Excessive formation of CaO through interaction with the laser results in the reaction with SiO_2 and formation of larnite according to Eq. (8):

$$2CaO + SiO_2 \rightarrow Ca_2SiO_4 \quad (8)$$

The formation of larnite is in agreement with the work done by Rashid et al. [31] where larnite was detected at Ca/Si molar ratios of 2:1 and 3:1 at 1450 °C, while at Ca/Si molar ratio of 1:1, the P–W phase was observed without larnite formation at any heating temperature. Semi-quantitative analysis (Fig. 3b) shows that the content of the elemental silicon decreases and calcium silicates increases in all samples as compared to the powder feedstock with lower HAp content. The weight percentage of P–W and larnite phases in sample 30/70_2 is 47.64 wt% and 20.11 wt%, respectively, while for sample 30/70_7 weight percentage of P–W is 8.03 wt% without larnite formation. As for the first feedstock, this can be explained by the time required for reactions to complete. Longer feedstock interaction with the laser (low scanning speed) results in a higher content of the formed calcium silicate phases.

3.2. Scaffold morphology

Scaffolds morphology depends on the process parameters (e.g. laser power, scanning speed, energy density) and used powder materials. The morphology of fabricated scaffolds was examined by SEM to determine the influence of process parameters onto the materials with different HAp and silicon phase content. The morphology of the scaffolds with 50 wt% of silicon and 50 wt% of HAp phase printed at different regimes are shown in Fig. 4. The pore size of 400 μm, according to the CAD model, are observed in 50/50_5, 50/50_6 and 50/50_7 scaffolds fabricated at the shortest exposure time, lowest laser current and energy density, and simultaneously with the highest scanning speed. Scaffolds 50/50_6 and 50/50_7 have shown the same morphology. The scaffolds (50/50_1) fabricated at the highest laser power and energy density, longest exposure time, and lowest scanning speed have smaller and non-uniform pore distribution and shape. An increased laser power and/or decreased scanning speed have reflective characteristics on energy density. This leads to a higher energy density and thus more temperature on the powder bed. The resulting higher thermal energy can eventually decrease the viscosity of the melt pool [32,33], resulting in the formation of enough large droplets and occupation of the pore volume as pointed by red arrows in Fig. 4. Therefore, the decreased pore volume is demonstrated by the scaffolds fabricated with the application of the highest laser power and the highest laser density. The cracks are evident at the samples produced at the shortest exposure times and lowest laser currents (the samples 50/50_1, 50/50_2 and 50/50_3), as depicted by green arrows in Fig. 4. Cracks can be the result of thermal stresses in the materials during processing.

The morphologies of the scaffolds with 30 wt% of silicon and 70 wt% of HAp phase fabricated at different printing parameters are shown in Fig. 5. Scaffolds 30/70_2 and 30/70_7 show the architecture in accordance with CAD design, while other scaffolds show structures with non-uniformly distributed pores on the surface.

The scaffolds fabricated at the lowest energy density and laser power have shown macropores of ~400 μm, which are in the best agreement with the CAD model and, henceforth, may be considered as the optimal

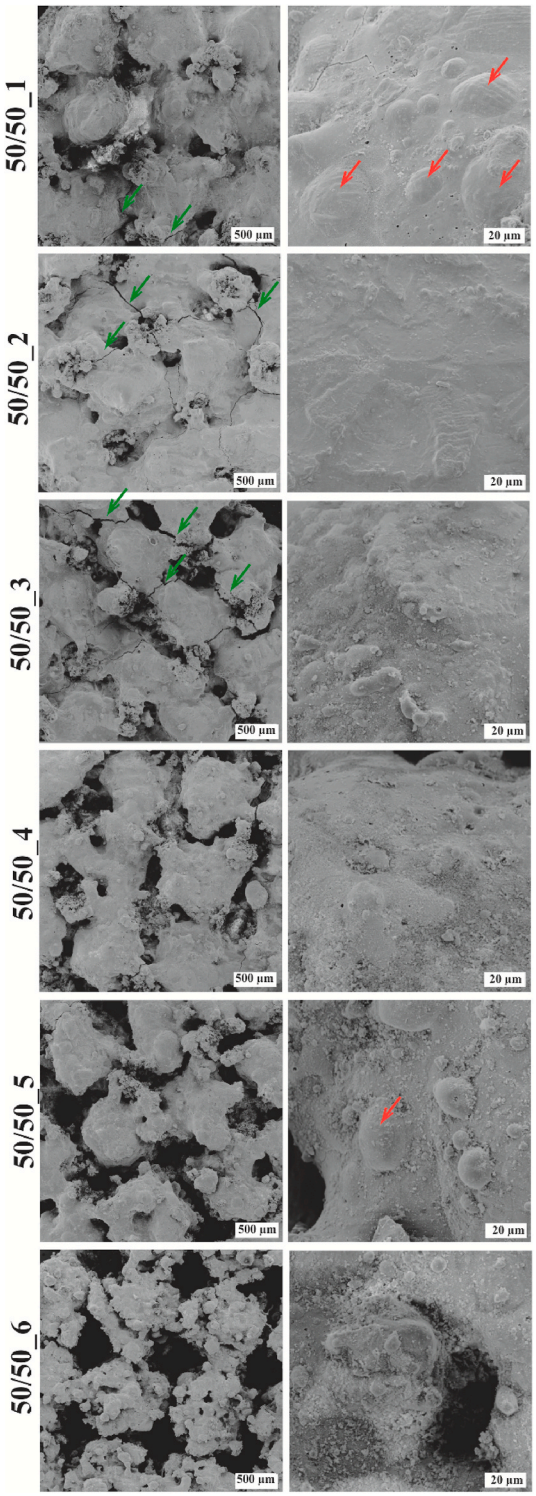

Fig. 4. SEM micrographs of the scaffolds with 50 wt% of silicon and 50 wt% of HAp phase fabricated at different printing parameters. Scale bar: 500 and 20 μm. (For interpretation of the references to colour in this figure legend, the reader is referred to the Web version of this article.)

product for further development and use. The laser power has a significant effect on the pore diameter of the scaffolds. The heat imparted by the laser to the melt pool on the scaffold fabricated with the highest laser power (1200 mA) tends to decrease the viscosity of the molten silicon and thus covering the pore of the scaffold as shown in 50/50_1 sample. Simultaneously, scaffold fabricated at lower laser power (500 mA) tends

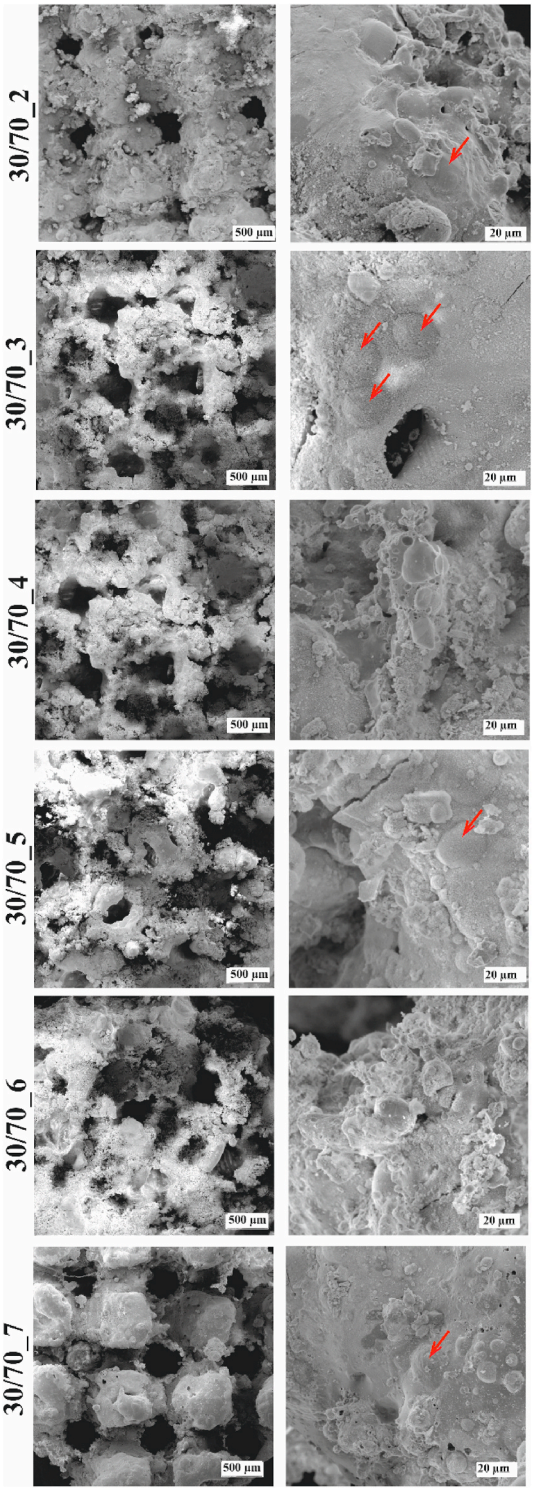

Fig. 5. SEM micrographs of the scaffolds with 30 wt% of silicon and 70 wt% of HAp phase fabricated at different printing parameters. Scale bar: 500 and 20 µm. (For interpretation of the references to colour in this figure legend, the reader is referred to the Web version of this article.)

to form a melt pool of higher viscosity constituting silicon, thus maintaining the pore size of the CAD model. The morphology of the fabricated scaffolds indicates the established interactions between silicon and bioactive particles after the SLM process. In the samples, the globular surface areas are evident as depicted (red) in Figs. 4 and 5. These globular areas can be annotated to balling effect. The balling effect is a predominant issue occurring due to capillary instability, marangoni convection and localized irregularities of the melt pool [33]. Balling effect results in disrupting the melt pool and break open the melt pool to the formation of spheres. However, these globular areas also indicate that the used laser energy is enough to melt the particles allowing its coalescence and forming the continuous silicon matrix in the final structure. From SEM micrographs, it is difficult to distinguish the interfaces indicating a good interaction between silicon and bioactive phases.

3.3. Compression test

The compressive strength of the fabricated scaffolds is illustrated in Fig. 6a, while morphologies of 50/50_1, 50/50_7, 30/70_2 and 30/70_6 scaffolds after compressive strength analysis are shown in Fig. 6b. As previously mentioned, at chosen processing parameters, scaffold 30/70_1 fabrication was not successful, while the compressive strength was not possible to be measured for the scaffold 30/70_7 due to the insufficient mechanical properties.

The highest compressive strength was observed for the scaffolds fabricated with the highest laser power which have shown smaller pore size (50/50_1 and 30/70_2) compared to the CAD model. The compressive force will be more concentrated on the main framework or skeleton of the scaffolds and very little on the open pores. Thus, it has yielded the highest compressive strength of ~18 MPa. This is followed by decreasing trend of the compressive strength of the scaffolds produced at a short exposure time, low laser current and high scanning speed. For instance, the scaffolds 50/50_6 and 50/50_7 have shown a good agreement to the CAD design and during the compression test, the bulk of the stress must have been concentrated on the open pores with more pore volume. It decreases the compressive strength of the scaffolds and thus yielding the value of 5 MPa. The compressive strength significantly decreased for all fabricated scaffolds compared to the 50/50_1 and 50/50_2 scaffolds. Scaffolds obtained from powders feedstock of 50 wt% of silicon and 50 wt% of HAp were composed of silicon and P–W. However, the compressive strength and weight percentages of obtained phases are not correlated. It can be concluded that the mechanical properties of the scaffolds are dependent on the printing parameters and resulting morphology. Similarly, a decreasing trend of the compressive strength values was determined for the scaffolds fabricated through second feedstock with higher HAp content starting from ~10 MPa for scaffold 30/70_2 to ~2 MPa for scaffold 30/70_6.

Considering phase content, morphology and compressive strength, the highly porous scaffold 30/70_2 containing 32.25 wt% of silicon, 20.11 wt% of larnite and 47.64 wt% of P–W with the compressive strength of ~10 MPa has been selected as the potential scaffold for the bone tissue engineering applications. In a study by Xu et al. [34], porous wollastonite scaffold has been *in vivo* studied for the bone regenerative and resorption capacity in a rabbit calvarial defect model by using porous β-TCP scaffolds as a control. Results have shown that wollastonite scaffolds have a higher resorption rate and induce more bone formation than the β-TCP scaffold. After 4 weeks of implantation, the area of newly formed bone in the wollastonite scaffold was ~14% of the total area and further increased to 28.36% at week 16. In contrast, the newly formed bone in porous β-TCP scaffold was much lower were at week 4 it reached 3.58% and 18.80% at week 16 [34]. The *in vivo* analysis of P–W was evaluated by De Aza et al. [35,36] through implantation into rat tibias. Results are in agreement with the results of porous wollastonite scaffolds reported by Xu et al. [34]. High-resolution transmission electron microscopy observations at the interface of the P–W scaffold and the host bone confirmed that the newly formed bone is composed of HAp-like nanocrystals growing epitaxially across the interface in the [002] direction [35]. In addition, it has been suggested that the release of Ca^{2+} ion from wollastonite leads to the formation of $Si–O^{-}$ active site on the surface of the scaffold that induces the nucleation of apatite, while the released Ca^{2+} ion enhances the apatite formation [36–38]. Wollastonite is the most extensively studied calcium

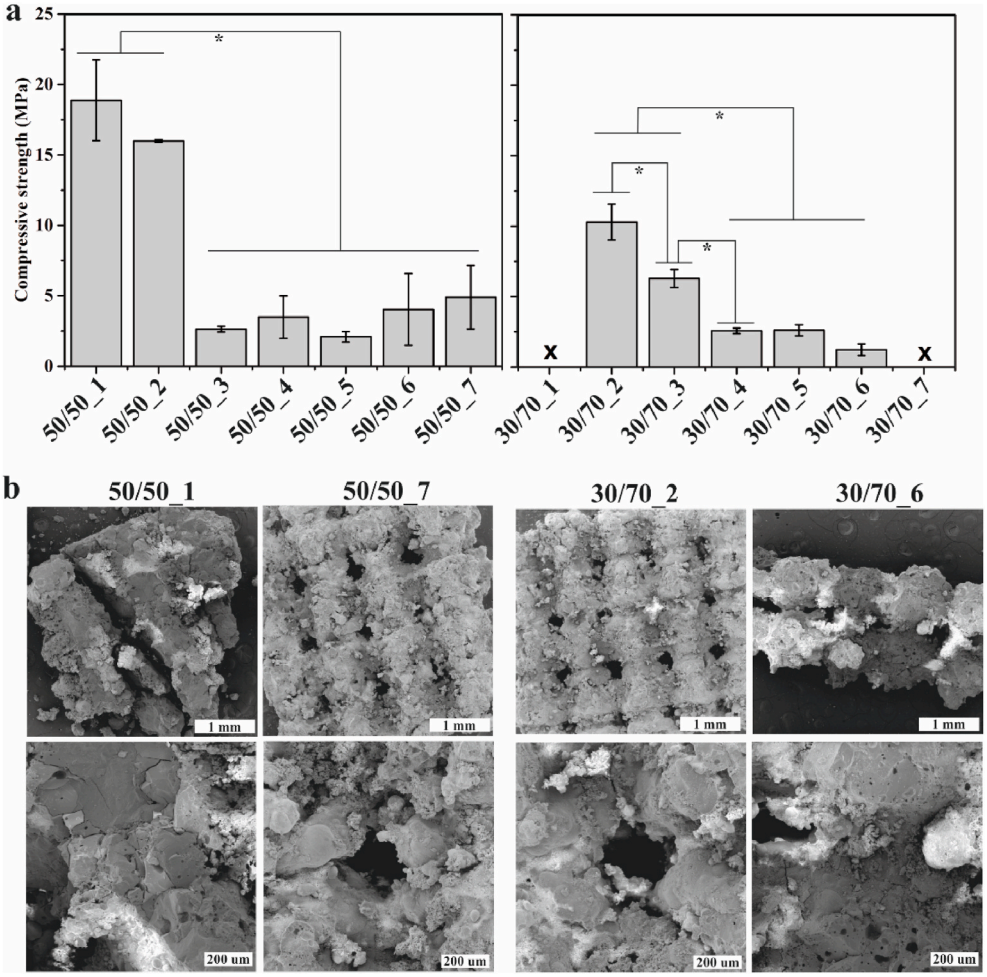

Fig. 6. The compressive strength of the fabricated scaffolds (a) and microstructures of 50/50_1, 50/50_7, 30/70_2 and 30/70_6 scaffolds after compressive strength analysis (b). Scale bar: 1 mm and 200 μm.

silicate due to its remarkable biomineralization ability; however, a higher degradation rate led to inadequate structural support to the damaged tissues while repairing bone disorders [38]. Therefore, selected scaffold 30/70_2 along with calcium silicates (P–W and larnite) contains 32.25 wt% of silicon that might ensure structural support during bone regeneration.

Optimisation of fabrication parameters for the SLM method was obtained for HAp and silicon feedstock. The 30/70_2 scaffold, produced from the powder feedstock containing 70 wt% of HAp and 30 wt% of silicon at the energy density of 166.0 J/mm^3, scanning speed 100.0 mm/s, laser current 1000 mA and exposure time 100 μs, undergoes *in situ* formation of P–W, larnite and silicon phases.

4. Conclusions

The present research investigated the influence of laser power on the silicon-hydroxyapatite powder feedstock. The silicon and calcium silicate scaffolds were manufactured by AM through the SLM approach using two powder feedstocks: (i) 50 wt% of HAp and 50 wt% of silicon, and (ii) 70 wt% of HAp and 30 wt% of silicon. The structures were fabricated according to the CAD model with a pore size of 400 μm at various processing parameters (energy density, scanning speed, laser current and exposure time). The feedstock of 50 wt% of HAp and 50 wt% of silicon results in *in situ* formation of P–W phase along with silicon, while an increase in feedstock HAp content, results in *in situ* formation of both P–W and larnite along with silicon phase. Even the HAp phase was decomposed under the influence of the laser to P–W and larnite in the presence of silicon, obtained bioactive phases will potentially lead to the precipitation of the HAp on the scaffolds *in vitro* and *in vivo*.

The designed pore size of 400 μm is a characteristic of the scaffolds produced at the shortest exposure time, and lowest laser current and energy density, and simultaneously at the highest scanning speed. The developed substrates can serve as a potential substitute for the metaphyseal region of long bones in bone tissue engineering; however, considering phase content, morphology and compressive strength, the highly porous scaffold 30/70_2 containing 32.25 wt% of silicon, 20.11 wt% of larnite and 47.64 wt% of P–W, with a compressive strength of ~10 MPa, has been selected for further studies. By using substituted HAp, along with obtained bioactive phases (P–W and larnite), a fabricated scaffold may contain homogenously distributed ions and/or associated bioactive phases. Further studies will be focused on the fabrication of 30/70_2 scaffold with the same process parameters by using HAp substituted with key role elements for bone regeneration like magnesium (Mg^{2+}), strontium (Sr^{2+}) and zinc (Zn^{2+}) ions.

Declaration of competing interest

The authors declare that they have no known competing financial interests or personal relationships that could have appeared to influence the work reported in this paper.

Acknowledgments

The authors are grateful for the JECS Trust for funding the visit of Dr. Antonia Ressler to Tallinn University of Technology (Contract No. 2020259). The L'Oreal-UNESCO Foundation 'For Women in Science', the European Regional Development Fund (grant KK.01.1.1.07.0014) and the Estonian Research Council (grant PRG643, I. Hussainova) are highly appreciated.

References

[1] W. Wang, K.W.K. Yeung, Bone grafts and biomaterials substitutes for bone defect repair: a review, Bioact. Mater. 2 (2017) 224–247, https://doi.org/10.1016/j.bioactmat.2017.05.007.
[2] G. Zhu, T. Zhang, M. Chen, K. Yao, X. Huang, B. Zhang, Y. Li, J. Liu, Y. Wang, Z. Zhao, Bone physiological microenvironment and healing mechanism: basis for future bone-tissue engineering scaffolds, Bioact. Mater. 6 (2021) 4110–4140, https://doi.org/10.1016/j.bioactmat.2021.03.043.
[3] I. Ratha, P. Datta, V.K. Balla, S.K. Nandi, B. Kundu, Effect of doping in hydroxyapatite as coating material on biomedical implants by plasma spraying method: a review, Ceram. Int. 47 (2021) 4426–4445, https://doi.org/10.1016/j.ceramint.2020.10.112.
[4] S. Zakeri, M. Vippola, E. Levänen, A comprehensive review of the photopolymerization of ceramic resins used in stereolithography, Addit. Manuf. 35 (2020), 101177, https://doi.org/10.1016/j.addma.2020.101177.
[5] N. Kamboj, A. Ressler, I. Hussainova, Bioactive ceramic scaffolds for bone tissue engineering by powder bed selective laser processing: a review, Materials 14 (2021) 5338, https://doi.org/10.3390/ma14185338.
[6] Y. Yang, G. Wang, H. Liang, C. Gao, S. Peng, L. Shen, C. Shuai, Additive manufacturing of bone scaffolds, Int. J. Bioprinting 5 (2019) 148, https://doi.org/10.18063/IJB.v5i1.148.
[7] Y. Lv, B. Wang, G. Liu, Y. Tang, E. Lu, K. Xie, C. Lan, J. Liu, Z. Qin, L. Wang, Metal material, properties and design methods of porous biomedical scaffolds for additive manufacturing: a review, Front. Bioeng. Biotechnol. 9 (2021), 641130, https://doi.org/10.3389/fbioe.2021.641130.
[8] N. Kamboj, J. Kazantseva, R. Rahmani, M.A. Rodríguez, I. Hussainova, Selective laser sintered bio-inspired silicon-wollastonite scaffolds for bone tissue engineering, Mater. Sci. Eng. C 116 (2020), 111223, https://doi.org/10.1016/j.msec.2020.111223.
[9] N. Kamboj, M. Aghayan, C.S. Rodrigo-Vazquez, M.A. Rodríguez, I. Hussainova, Novel silicon-wollastonite based scaffolds for bone tissue engineering produced by selective laser melting, Ceram. Int. 45 (2019) 24691–24701, https://doi.org/10.1016/j.ceramint.2019.08.208.
[10] C. Sara Rodrigo-Vázquez, Nikhil Kamboj, Marina Aghayan, Ada Sáeza, Antonio H. De Aza, Miguel A. Rodríguez, I. Hussainova, Manufacturing of silicon – bioactive glass scaffolds by selective laser melting for bone tissue engineering, Ceram. Int. (2020), https://doi.org/10.1016/j.ceramint.2020.07.171.
[11] W. Sun, J.E. Puzas, T.J. Sheu, X. Liu, P.M. Fauchet, Nano-to microscale porous silicon as a cell interface for bone-tissue engineering, Adv. Mater. 19 (2007) 921–924, https://doi.org/10.1002/adma.200600319.
[12] M.Q. Arumugam, D.C. Ireland, R.A. Brooks, N. Rushton, W. Bonfield, Orthosilicic acid increases collagen type I mRNA expression in human bone-derived osteoblasts in vitro, Key Eng. Mater. 254 (2006) 869–872. 10.4028/www.scientific.net/KEM.254-256.869.
[13] E.M. Carlisle, C. Suchil, Silicon and ascorbate interaction in cartilage formation in culture, Fed. Proc. 42 (1983) 398.
[14] H. Li, J. Chang, Bioactive silicate materials stimulate angiogenesis in fibroblast and endothelial cell co-culture system through paracrine effect, Acta Biomater. 9 (2013) 6981–6991, https://doi.org/10.1016/j.actbio.2013.02.014.
[15] S.G. Romeo, K.M. Alawi, J. Rodrigues, A. Singh, A.P. Kusumbe, S.K. Ramasamy, Endothelial proteolytic activity and interaction with non-resorbing osteoclasts mediate bone elongation, Nat. Cell Biol. 21 (2019) 430–441, https://doi.org/10.1038/s41556-019-0304-7.
[16] W.J. Landis, D.D. Lee, J.T. Brenna, S. Chandra, G.H. Morrison, Detection and localization of silicon and associated elements in vertebrate bone tissue by imaging ion microscopy, Calcif. Tissue Int. 38 (1986) 52–59, https://doi.org/10.1007/BF02556595.
[17] E. Boanini, M. Gazzano, A. Bigi, Ionic substitutions in calcium phosphates at low temperature, Acta Biomater. 6 (2010) 1882–1894, https://doi.org/10.1016/j.actbio.2009.12.041.
[18] J.R. Henstock, L.T. Canham, S.I. Anderson, Silicon: the evolution of its use in biomaterials, Acta Biomater. 11 (2015) 17–26, https://doi.org/10.1016/j.actbio.2014.09.025.
[19] A. Ressler, A. Žužić, I. Ivanišević, N. Kamboj, H. Ivanković, Ionic substituted hydroxyapatite for bone regeneration applications: a Review, Open Ceramics 6 (2021), 100122, https://doi.org/10.1016/j.oceram.2021.100122.
[20] C. Shuai, Y. Nie, C. Gao, P. Feng, J. Zhuang, Y. Zhou, S. Peng, The microstructure evolution of nanohydroxapatite powder sintered for bone tissue engineering, J. Exp. Nanosci. 8 (2013) 762–773, https://doi.org/10.1080/17458080.2011.606507.
[21] C. Shuai, C. Gao, Y. Nie, H. Hu, Y. Zhou, S. Peng, Structure and properties of nano-hydroxypatite scaffolds for bone tissue engineering with a selective laser sintering system, Nanotechnology 22 (2011), 285703, https://doi.org/10.1088/0957-4484/22/28/285703.
[22] N.K. Kamboj, M.A. Rodriguez, R. Rahmani, K.G. Prashanth, I. Hussainova, Bioceramic scaffolds by additive manufacturing for controlled delivery of the antibiotic vancomycin, Proc. Est. Acad. Sci. 68 (2) (2019) 185–190, https://doi.org/10.3176/proc.2019.2.10.
[23] L.J. Vaselinović, L.J. Karanović, Z. Stojanović, I. Bračko, S. Marković, N. Ignjatović, D. Uskoković, Crystal structure of cobalt-substituted calcium hydroxyapatite nanopowders prepared by hydrothermal processing, J. Appl. Crystallogr. 43 (2010) 320–327, https://doi.org/10.1107/S0021889809051395.
[24] A.D. Elliot, Structure of pyrrhotite 5C (Fe_9S_{10}), Acta Crystallogr. B 66 (2010) 271–279, https://doi.org/10.1107/S0108768110011845.
[25] H. Yang, C.T. Prewitt, On the crystal structure of pseudowollastonite ($CaSiO_3$), Am. Mineral. 84 (1999) 929–932, https://doi.org/10.2138/am-1999-5-629.
[26] T. Tsurumi, Y. Hirano, H. Kato, T. Kamiya, M. Daimon, Crystal structure and hydration of belite locality, Ceram. Trans. 40, 19-25.
[27] M. Casas-Luna, Mariano, M. Horynová, S. Tkachenko, L. Klakurková, L. Celko, S. Diaz-de-la-Torre, E.B. Montufar, Chemical stability of tricalcium phosphate–iron composite during spark plasma sintering, J. Compos. Sci. 2 (2018) 51, https://doi.org/10.3390/jcs2030051.
[28] H.A. Santos, Porous Silicon for Biomedical Applications, first ed., Elsevier, 2014.
[29] J.C. Elliott, Structure and Chemistry of the Apatites and Other Calcium Orthophosphates, first ed., Elsevier Science, Amsterdam, 1994.
[30] Q. Liu, W. Liu, L. Lv, R. Li, B. Liang, H. Yue, S. Tang, C. Li, Study on reactions of gaseous P_2O_5 with $Ca_3(PO_4)_2$ and SiO_2 during a rotary kiln process for phosphoric acid production, Chin. J. Chem. Eng. 26 (2018) 795–805, https://doi.org/10.1016/j.cjche.2017.11.016.
[31] R.A. Rashid, R. Shamsudin, M.A.A. Hamis, A. Jalar, Low temperature production of wollastonite from limestone and silica sand through solid-state reaction, J. Asian Ceram. Soc. 2 (2014) 77–81, https://doi.org/10.1016/j.jascer.2014.01.010.
[32] S. Liu, H. Guo, Balling behavior of selective laser melting (SLM) magnesium alloy, Materials 13 (2020) 3632, https://doi.org/10.3390/ma13163632.
[33] N.K. Tolochko, S.E. Mozzharov, I.A. Yadroitsev, T. Laoui, L. Froyen, V.I. Titov, M. B. Ignatiev, Balling processes during selective laser treatment of powders, Rapid Prototyp. J. 10 (2004) 78–87, https://doi.org/10.1108/13552540410526953.
[34] S. Xu, K. Lin, Z. Wang, J. Chang, L. Wang, J. Lu, C. Ning, Reconstruction of calvarial defect of rabbits using porous calcium silicate bioactive ceramics, Biomaterials 29 (2008) 2588–2596, https://doi.org/10.1016/j.biomaterials.2008.03.013.
[35] P.N. de Aza, Z.B. Luklinska, A. Martinez, M.R. Anseau, F. Guitian, S. De Aza, Morphological and structural study of pseudowollastonite implants in bone, J. Microsc. 197 (2000) 60–67, https://doi.org/10.1046/j.1365-2818.2000.00647.x.
[36] W. Cao, L.L. Hench, Bioactive materials, Ceram. Int. 22 (1996) 493–507, https://doi.org/10.1016/0272-8842(95)00126-3.
[37] V. Rubio, P. Mazón, M.A. de la Casa-Lillo, P.N. De Aza, Preparation, characterization and in vitro behavior of a new eutectoid bioceramic, J. Eur. Ceram. Soc. 35 (2015) 317–328, https://doi.org/10.1016/j.jeurceramsoc.2014.08.039.
[38] S.K. Venkatraman, R. Choudhary, G. Krishnamurithy, H.R. Balaji Raghavendran, M.R. Murali, T. Kamarul, A. Suresh, J. Abraham, S. Swamiappan, Biomineralization, mechanical, antibacterial and biological investigation of larnite and rankinite bioceramics, Mater. Sci. Eng. C 118 (2021), 111466, https://doi.org/10.1016/j.msec.2020.111466.